Progress in Flight Physics **9** (2017) 409-420
DOI: 10.1051/eucass/201709409

SIMULATION OF HYPERSONIC SHOCK WAVE – LAMINAR BOUNDARY LAYER INTERACTIONS

N. Kianvashrad and D. Knight

Rutgers, The State University of New Jersey
New Brunswick, NJ 08903, USA

The capability of the Navier–Stokes equations with a perfect gas model for simulation of hypersonic shock wave – laminar boundary layer interactions is assessed. The configuration is a hollow cylinder flare. The experimental data were obtained by Calspan-University of Buffalo (CUBRC) for total enthalpies ranging from 5.07 to 21.85 MJ/kg. Comparison of the computed and experimental surface pressure and heat transfer is performed and the computed flowfield structure is analyzed.

1 INTRODUCTION

Flight at hypersonic speeds generates strong shock waves due to the changes in the vehicle surface geometry. The interaction of shock waves with the vehicle boundary layer can result in boundary layer separation and concommitant high heat transfer and surface pressure at reattachment. The aerodynamic design of efficient and reliable hypersonic vehicles thus requires careful consideration of such shock wave – boundary layer interactions.

During the past several decades, there has been extensive computational, experimental, and theoretical research on hypersonic shock wave – boundary layer interactions for both laminar and turbulent boundary layers. The capability of Computational Fluid Dynamics (CFD) to accurately predict these flows has been widely examined. Examples include Knight *et al.* [1], Schmisseur [2], Candler [3], and Gaitonde [4].

Recently, CUBRC performed a series of experiments for hypersonic shock wave – boundary layer interactions for laminar and turbulent boundary layers. The experiments were conducted for a range of stagnation enthalpies from 5.07 to 21.85 MJ/kg to provide a matrix of test cases for assessment of CFD capability. An initial "blind" comparison of CFD predictions and experiments was presented at the AIAA Aviation 2014 meeting [5, 6].

The objective of this paper is the assessment of CFD modeling of hypersonic shock wave – laminar boundary layer interactions using the Navier–Stokes

equations and assuming a perfect gas. The simulations are compared with the experimental data from CUBRC.

2 DESCRIPTION OF EXPERIMENT

The experimental model, shown in Fig. 1, has an overall length of 220 mm. The instrumentation includes 16 to 18 pressure transducers and 48 to 51 heat transfer gauges depending on the test. A total of five separate tests were performed in the LENS XX expansion tunnel at stagnation enthalpies from 5.07 to 21.85 MJ/kg and Mach numbers from 11.3 to 13.2 (Table 1). The gas was air at full chemical and thermochemical equilibrium with mass fractions of 0.765 and 0.235 for N_2 and O_2, respectively. The model surface was isothermal at 300 K. The details of the LENS XX facility are presented in [7, 8].

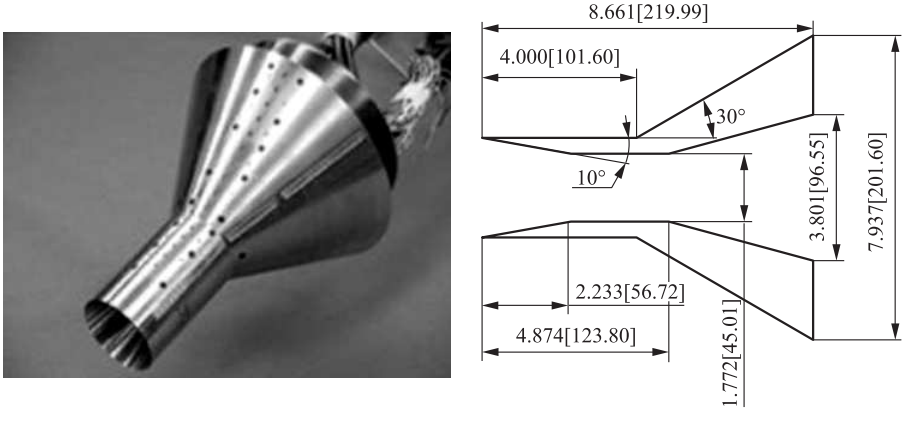

(*a*) (*b*)

Figure 1 Small hollow cylinder flare: (*a*) instrumentation; and (*b*) geometry. Dimensions are in inches [millimeters]

Table 1 Freestream conditions

Run No.	Total enthalpy, MJ/kg	Mach number	Pitot pressure, kPa	Unit Reynolds, 10^6 m^{-1}	Velocity, km/s	Density, g/m^3	Temperature, K
1	5.07	11.3	5.9	0.15	3.123	0.634	189
2	10.43	12.6	9.7	0.12	4.497	0.499	318
3	11.25	11.9	36.5	0.37	4.660	1.750	383
4	15.54	11.5	64.0	0.42	5.470	2.216	569
5	21.85	13.2	39.0	0.20	6.515	0.947	618

3 METHODOLOGY

Although the stagnation enthalpies of the experiments (see Table 1) are well within the range for nonequilibrium effects to be significant, let us assume a perfect gas model together with the laminar Navier–Stokes equations in order to indirectly assess the effect of nonequilibrium thermochemistry for this configuration. Using the Einstein summation notation,

$$\frac{\partial \rho}{\partial t} + \frac{\partial \rho u_j}{\partial x_j} = 0\,;$$

$$\frac{\partial \rho u_i}{\partial t} + \frac{\partial \rho u_i u_j}{\partial x_j} = -\frac{\partial p}{\partial x_i} + \frac{\partial \tau_{ij}}{\partial x_j}\,;$$

$$\frac{\partial \rho \varepsilon}{\partial t} + \frac{\partial}{\partial x_j}\left(\rho \varepsilon + p\right) u_j = -\frac{\partial q_j}{\partial x_j} + \frac{\partial \tau_{ij} u_i}{\partial x_j}\,;$$

$$p = \rho R T$$

where the total energy per unit mass ε is

$$\varepsilon = e + \frac{1}{2} u_j u_j\,;$$

the internal energy per unit mass e is

$$e = c_v T\,;$$

and the heat flux vector and laminar viscous stress tensor are

$$q_j = -k \frac{\partial T}{\partial x_j}\,;$$

$$\tau_{ij} = -\frac{2}{3} \mu \frac{\partial u_k}{\partial x_k} \delta_{ij} + \mu \left(\frac{\partial u_i}{\partial x_j} + \frac{\partial u_j}{\partial x_i} \right).$$

The molecular viscosity μ is defined by Sutherland's law and the molecular Prandtl number $\mathrm{Pr} = \mu c_p / k$ is 0.72. The gas constant $R = 287$ J/(kg·K) for air.

The computations were performed using the GASPex code [9]. The inviscid fluxes' discretization used Roe's and Van Leer's methods with Min-Mod reconstruction. Viscous fluxes were discretized using central differencing. A block-structured grid was generated in 6 zones as indicated in Fig. 2. The boundary conditions are extrapolation from A to B, inflow from B to C, symmetry from C to D, inflow from D to E, symmetry from E to F, inflow from F to G, symmetry from G to H, extrapolation from H to I, and isothermal no-slip wall from I to J and then to A. The simulations were initialized using the freestream conditions and converged to steady state using Gauss–Seidel iteration [9]. The

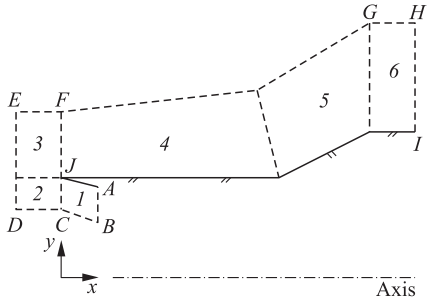

Figure 2 Computational domain

Table 2 Computational grid (i_l — number of points along the surface and j_l — number of points away from the surface)

Region	i_l	j_l	Δx, μm	$\Delta y_{\min}$, μm
1	81	321	25.00	6.25
2	81	321	25.00	6.25
3	81	1601	25.00	6.25
4	4065	1601	25.00	6.25
5	5465	1601	21.67	6.25
6	801	1601	25.00	6.25

details of the finest computational grid are presented in Table 2 corresponding to $16.7 \cdot 10^6$ cells. A grid sequencing method was employed to create a succession of grids with $1.04 \cdot 10^6$ cells (coarse grid), $4.18 \cdot 10^6$ cells (medium grid), and $16.7 \cdot 10^6$ cells (fine grid) for Run Nos. 1, 2, 4, and 5 in Table 1.

4 RESULTS

4.1 Comparison with Experiment

The computed surface pressure and heat transfer are compared with experiment in Figs. 3 to 6. The results are shown for all three grids (coarse, medium, and fine) with the exception of Run 5 where the results are presented for coarse and medium grids only.

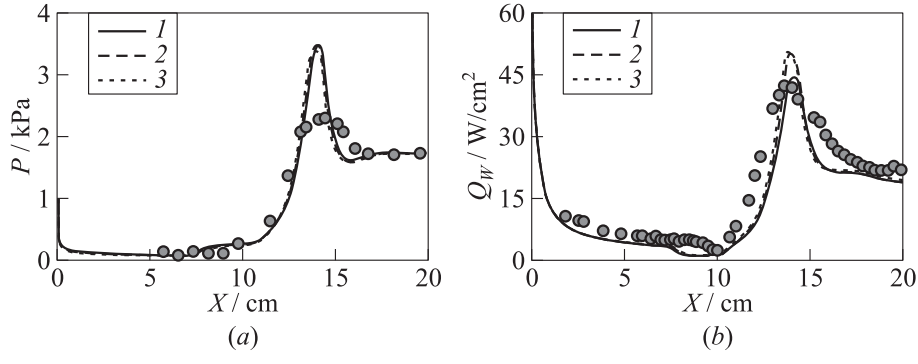

Figure 3 Surface pressure (a) and heat transfer (b) for Run 1 (5.07 MJ/kg): *1* — coarse grid; *2* — medium grid; and *3* — fine grid. Signs refer to experiments and curves to calculations

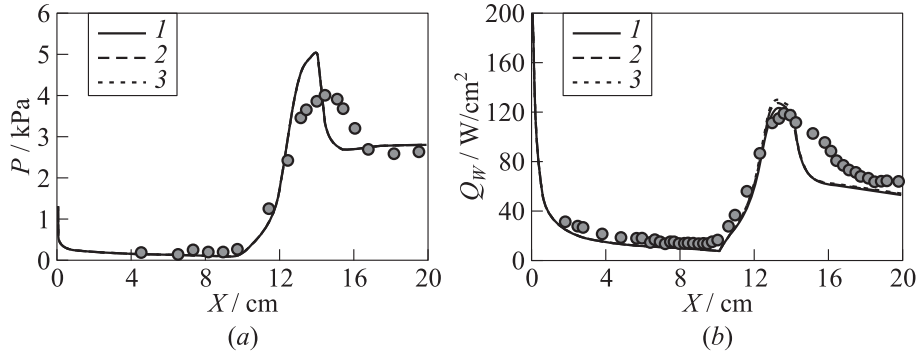

Figure 4 Surface pressure (a) and heat transfer (b) for Run 2 (10.43 MJ/kg): *1* — coarse grid; *2* — medium grid; and *3* — fine grid. Signs refer to experiments and curves to calculations

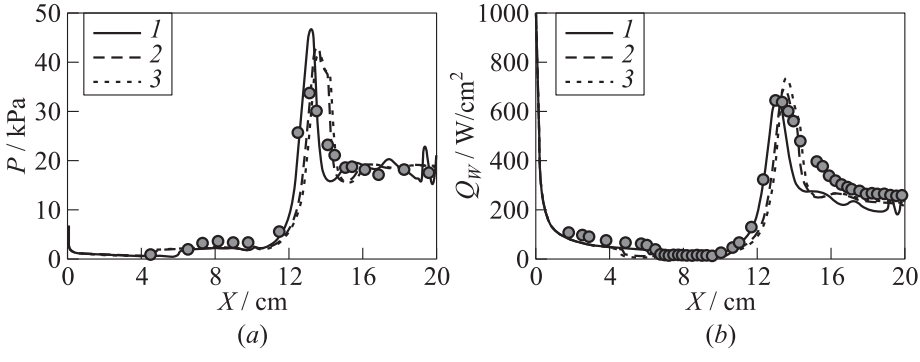

Figure 5 Surface pressure (a) and heat transfer (b) for Run 4 (15.54 MJ/kg): *1* — coarse grid; *2* — medium grid; and *3* — fine grid. Signs refer to experiments and curves to calculations

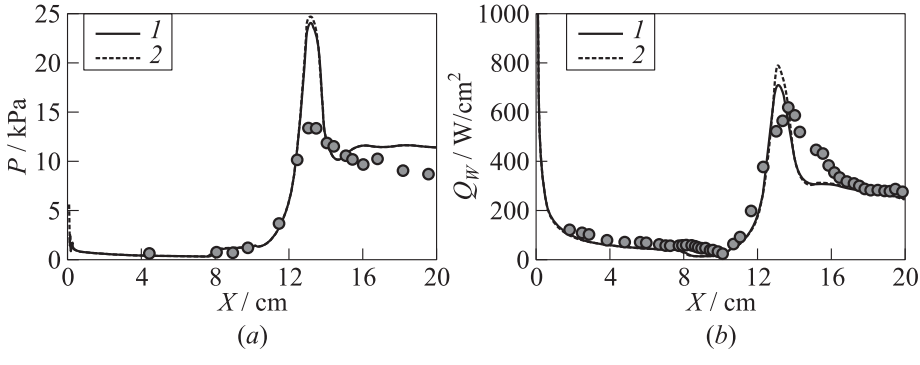

Figure 6 Surface pressure (a) and heat transfer (b) for Run 5 (21.85 MJ/kg): *1* — coarse grid; and *2* — medium grid. Signs refer to experiments and curves to calculations

Run 1 (5.07 MJ/kg)

The computed surface pressure (see Fig. 3*a*) shows good agreement with experiment in the interaction region except that the peak pressure exceeds the experiment by 60%. The computed surface heat transfer (see Fig. 3*b*) agrees closely with experiment, including prediction of the peak heat transfer within the experimental uncertainty (±10%); however, the computed separation point is farther upstream than in the experiment and the recovery downstream of reattachment is more rapid than in the experiment.

Run 2 (10.43 MJ/kg)

The computed surface pressure (see Fig. 4*a*) shows similar good agreement with experiment in the interaction region; however, the peak pressure exceeds the experiment by 30%. The computed surface heat transfer (see Fig. 4*b*) agrees closely with experiment, including prediction of the peak heat transfer within the experimental uncertainty. As before, the recovery downstream of reattachment is more rapid than in the experiment.

Run 4 (15.54 MJ/kg)

The computed surface pressure (see Fig. 5*a*) is in good agreement with experiment, although the peak pressure exceeds the experiment by 23%. The computed surface heat transfer (see Fig. 5*b*) shows good agreement with experiment, again including prediction of the peak heat transfer within the experimental uncertainty. As before, a more rapid recovery downstream of reattachment is observed compared to the experiment.

Run 5 (21.85 MJ/kg)

The computed surface pressure (see Fig. 6*a*) displays good agreement with experiment in the interaction, except the peak pressure exceeds the experiment by 87%. The computed surface heat transfer (see Fig. 6*b*) again shows good agreement with experiment, including prediction of the peak heat transfer within 25% of the experimental value. A consistent more rapid recovery downstream of reattachment is observed compared to the experiment.

Discussion of Comparison with Experiment

Conventional wisdom would indicate that a nonequilibrium thermochemistry model would be necessary to accurately predict the aerothermodynamic loads (i. e., surface pressure and heat transfer) for shock wave – laminar boundary layer interactions at high enthalpy/hypersonic conditions. Therefore, it is indeed quite surprising that a *perfect gas* model (coupled with the laminar Navier–Stokes

equations) can accurately predict the peak heat transfer in these shock wave–laminar boundary layer interactions to within the experimental uncertainty up to 15.54 MJ/kg and within approximately twice the experimental uncertainty at 21.85 MJ/kg.

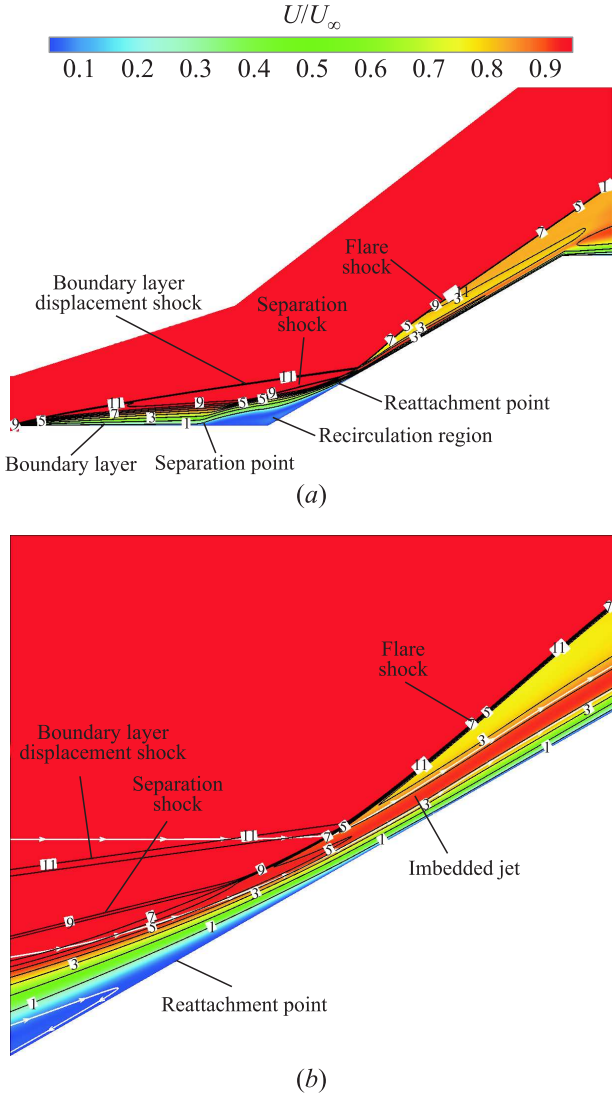

Figure 7 Velocity contours and Mach number levels for Run 1 (5.07 MJ/kg)

A complete answer to this paradox requires comparison with simulations incorporating nonequilibrium thermochemistry model(s) and such research is in progress.

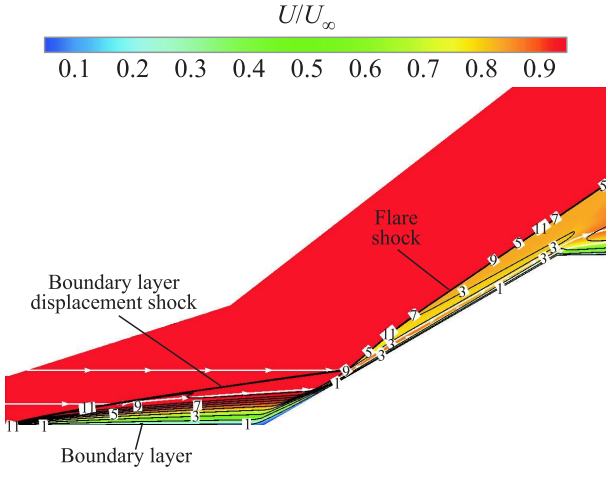

(*a*)

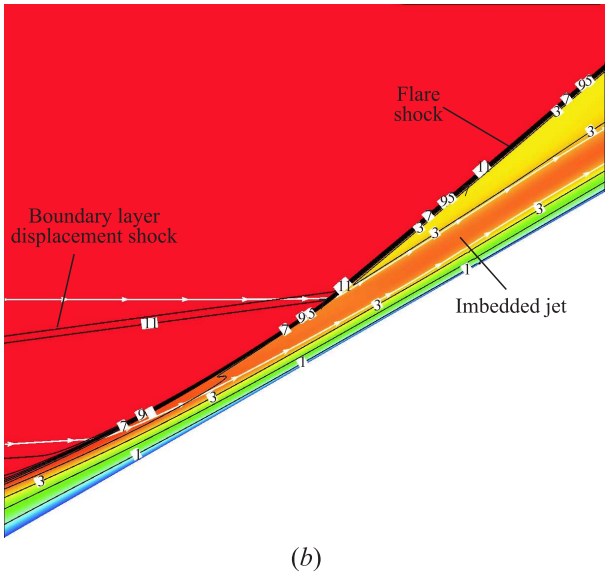

(*b*)

Figure 8 Velocity contours and Mach number levels for Run 2 (10.43 MJ/kg)

4.2 Flowfield Structure

The computed flowfield structure for the 4 cases is presented in Figs. 7 to 10. The principal features are similar for all four cases. Figure 7*a* displays the contours

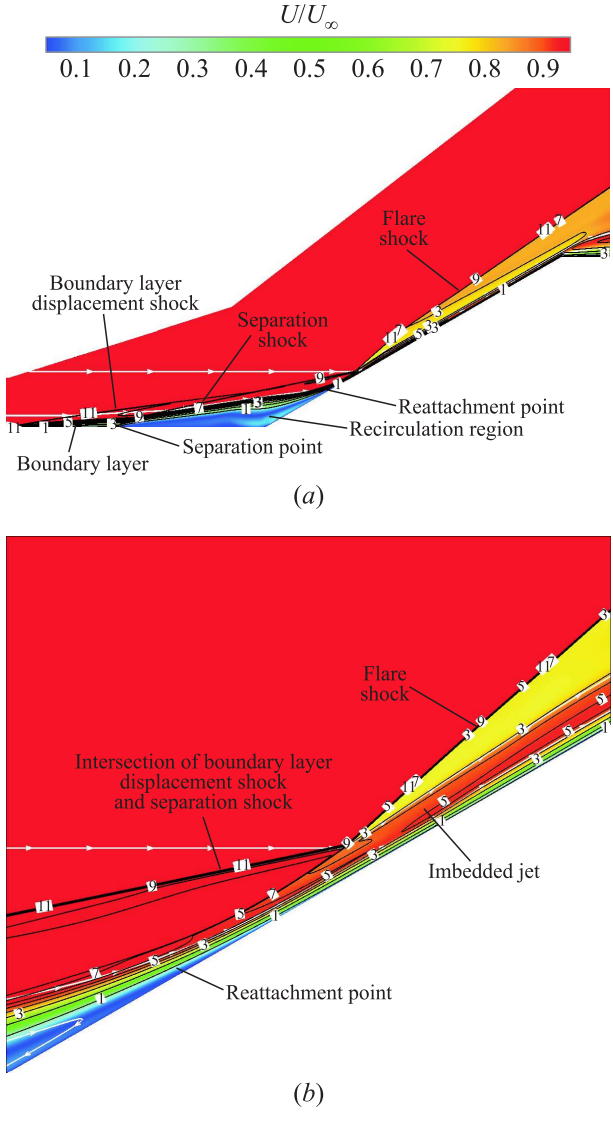

Figure 9 Velocity contours and Mach number levels for Run 4 (15.54 MJ/kg)

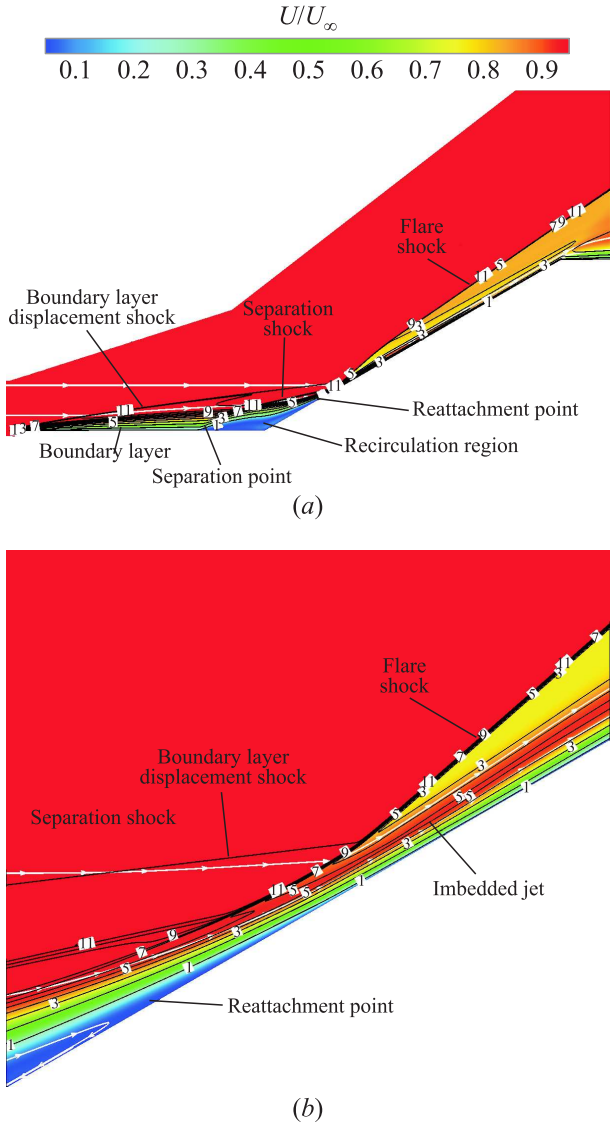

Figure 10 Velocity contours and Mach number levels for Run 5 (21.85 MJ/kg)

of the normalized velocity U/U_∞ where $U = \sqrt{u_j u_j}$. The displacement thickness of the boundary layer on the cylinder generates a weak shock ("Boundary layer displacement shock"). The adverse pressure gradient due to the flare causes a separation for Run 1 (see Fig. 7), Run 4 (see Fig. 9), and Run 5 (see Fig. 10);

however, no separation is observed for Run 2 (see Fig. 8). The size of the separation region varies due to the freestream conditions (i. e., total enthalpy, Mach number, and Reynolds number) indicated in Table 1. A particularly interesting feature is the formation of an imbedded supersonic jet within the boundary layer downstream of the location of peak pressure as indicated in Figs. 7*b* to 10*b*. The boundaries of the jet are denoted by white streamlines, and the entrained freestream flow that forms the imbedded supersonic jet are indicated in Figs. 7*a* to 10*a*. The entrained freestream flow traverses three successive shocks (i. e., boundary layer displacement shock, separation shock, and flare shock) resulting in a lower entropy (and higher velocity) than the flow traversing the flare shock alone and, hence, forming the imbedded supersonic jet.

5 CONCLUDING REMARKS

The capability of the Navier–Stokes equations with a perfect gas model to simulate hypersonic shock wave – laminar boundary layer interactions is assessed by comparison with experimental data from CUBRC for a hollow cylinder flare model. The total enthalpies range from 5.07 to 21.85 MJ/kg. The computed surface pressure shows good agreement with experiment within the interaction although the peak pressure is significantly overpredicted. Most surprisingly, the peak heat transfer is accurately predicted to within experimental uncertainty for the cases with total enthalpies from 5.07 to 15.54 MJ/kg and within 25% for the highest enthalpy case (21.85 MJ/kg). The computed flowfield shows a complex shock interaction structure and the formation of an imbedded supersonic jet within the boundary layer downstream of the location of peak pressure.

ACKNOWLEDGMENTS

The research was sponsored by the U.S. Office of Naval Research under Grant No. N00014-14-1-0827. The program manager is Gil Graff.

REFERENCES

1. Knight, D., J. Longo, D. Drikakis, D. Gaitonde, A. Lani, I. Nompelis, B. Reimann, and L. Walpot. 2012. Assessment of CFD capability for prediction of hypersonic shock interactions. *Prog. Aerosp. Sci.* 48-49:8–26.
2. Schmisseur, J. 2015. Hypersonics into the 21st century: A perspective on AFOSR-sponsored research in aerothermodynamics. *Prog. Aerosp. Sci.* 72:3–16.

3. Candler, G. 2015. Rate-dependent energetic processes in hypersonic flow. *Prog. Aerosp. Sci.* 72:37–48.
4. Gaitonde, D. 2015. Progress in shock wave/boundary layer interactions. *Prog. Aerosp. Sci.* 72:80–99.
5. MacLean, M., M. Holden, and A. Dufrene. 2014. Comparison between CFD and measurements for real-gas effects on laminar shock wave boundary layer interaction, I. *AIAA Aviation*. Atlanta, GA.
6. Wadhams, T., M. Holden, and M. MacLean. 2014. Comparison of experimental and computational results from 'blind' turbulent shock wave interaction study over cone flare and hollow cylinder flare configuration. *AIAA Aviation*. Atlanta, GA.
7. Dufrene, A., M. MacLean, R. Parker, T. Wadhams, E. Mundy, and M. Holden. 2010. Characterization of the new lens expansion tunnel facility. AIAA Paper No. 2010-1564.
8. Dufrene, A., M. MacLean, R. Parker, and M. Holden. 2011. Experimental characterization of the lens expansion tunnel facility including blunt body surface heating. AIAA Paper No. 2011-626.
9. Gaspex version 5.1.2 reference guide. 2014. Blacksburg, VA: Aerosoft, Inc.